lubricants

MDPI

Article

Sustainable Vegetable Oil-Based Minimum Quantity Lubrication Assisted Machining of AZ91 Magnesium Alloy: A Grey Relational Analysis-Based Study

Assem Alshibi, Abdelrahman Nasreldin and Salman Pervaiz [1,*]

Department of Mechanical and Industrial Engineering, Rochester Institute of Technology—Dubai Campus, Dubai P.O. Box 341055, United Arab Emirates

* Correspondence: sxpcad@rit.edu; Tel.: +971-4-371-2036

Abstract: The implementation of magnesium alloys in a multitude of industries has been proven to be a mere effect of their attractive light weight, corrosion resistant, and biodegradable properties. These traits allow these materials to portray an excellent sustainable machinability. However, with increasing demand, it is essential to explore sustainable means of increasing production while mitigating reductions in sustainability. The current work aims to assess and optimize the high-speed machinability of AZ91 with the use of a vegetable oil-based minimum quantity lubrication (MQL) system using the grey relational analysis (GRA) on the basis of chip morphology and tool wear. The investigation entailed a full factorial design with MQL flow rate, cutting speed, and feed rate as the control parameters and flank wear, land width, chip contact length, saw-tooth pitch, chip segmentation ratio, chip compression ratio, and shear angle as the output responses. The optimal control parameters predicted and experimentally confirmed were an MQL flow rate of 40 mL/h, cutting speed of 300 m/min, and feed rate of 0.3 mm/rev. The usage of said optimal parameters results in a grey relational grade improvement of 0.2675 in comparison to the referenced first experimental run. Moreover, the MQL flow rate was regarded as the critical variable with a contribution percentage of 20% for the grey relational grade.

Keywords: MQL; orthogonal turning; magnesium alloy; AZ91; chip morphology

Citation: Alshibi, A.; Nasreldin, A.; Pervaiz, S. Sustainable Vegetable Oil-Based Minimum Quantity Lubrication Assisted Machining of AZ91 Magnesium Alloy: A Grey Relational Analysis-Based Study. *Lubricants* **2023**, *11*, 79. https://doi.org/10.3390/lubricants11020079

Received: 13 December 2022
Revised: 2 February 2023
Accepted: 8 February 2023
Published: 12 February 2023

1. Introduction

The demand for magnesium alloys is on a continuous upward trend in industries, such as automotive [1,2], biomedical [3–5], and aerospace [6,7]. This is due to the alloys' appealing light weight [8], biodegradability [9], corrosion resistance [10], and high specific strength [11]. In regard to similar light weight alloys, magnesium alloys are softer than most aluminium and titanium alloys [12] resulting in lower cutting energy requirements. Moreover, due to the prefaced softness, an excellent surface finish is easily achievable. However, in the literature, their general machinability assessment is scarce and limited in comparison to other conventional alloys.

Viswanathan et al. [13] aimed to investigate the varying effects of the cutting parameters on the machinability indicators of AZ91D in dry turning. A grey relational analysis (GRA) was conducted to optimize the cutting parameters based on cutting forces, flank wear, surface roughness, and material removal rate (MRR). Increased cutting forces and flank wear evolution were noted at elevated feed rates and cut depths. Additionally, increased cutting speeds led to minor increases in flank wear land width. The build-up of the workpiece material on the tool, due to adhesion, was noted as a large contributor of the tool wear evolution. However, better surface quality was noted at elevated cutting speeds and deteriorated with increasing feed rate and cut depth. The depth of the cut and feed rate were closely tied and regarded as the most influential input parameters. A similar investigation was carried out by Shi et al. [14] who monitored cutting forces, surface quality,

and chip morphology during the dry end-milling of AZ91D. Cutting forces were inversely related to cutting speed, while elevated cutting forces were noted at higher feed rates. Corollary effects can be seen on the chip morphology since higher feed rates resulted in the formation of loose and damaged saw-tooth chips which were attributed to the intense shearing. Moreover, cutting speed was found to the main influencing parameter of chip length with higher cutting speeds resulting in longer curly chip segments.

Generally, during the machining of magnesium alloys, the main reported mechanism of tool wear is adhesion. This is usually signified by the excessive amounts of built-up edge (BUE) and built-up layer (BUL) along the cutting tool. A study by Ramesh et al. [15] was aimed at investigating and optimizing the cutting parameters and their effects of tool wear evolution and surface roughness during the dry turning of AZ91D. An increase in any of the cutting parameters resulted in a progressive increase of tool wear and surface roughness, with the feed rate ranked as the critical parameter. A more tool-wear centred study was conducted by Tönshoff and Winkler [16] who investigated the effects of varying tool coating materials on BUL formation, cutting forces, and surface roughness during the high-speed dry turning of AZ91HP. Polycrystalline diamond (PCD) and titanium nitride (TiN) coated tools were utilized along a set of constant machining parameters. Large amounts of adhered material, in the form of BUL/BUE, were noted on the TiN cutting tool as a result of the elevated cutting temperatures. Cutting forces were relatively constant through the first half of the cutting length and portrayed an aggressive oscillatory behaviour towards the end of the cutting length. This was attributed to the excessive formation of BUE/BUL that resulted in the alteration of the cutting-edge geometry.

The prevailing occurrence of adhesion during the machining of magnesium alloys can also be seen in other machining processes, such as drilling. Wang et al. [17] aimed to map the wear progression mechanisms to the cutting parameters during the dry drilling of AZ91 magnesium alloy. Using an HSS drilling tool, a large range of cutting speeds and feed rates were tested and the wear map was developed and contained adhesive wear, diffusion wear, and abrasive wear. The combinations of low speed and high feed, as well as high speed and low feed resulted in regions of abrasive wear. Similarly, the review compiled by Carou et al. [18] emphasized the presence of adhered material and its setbacks. Another indicator for the occurrence of friction that affects tool life is tool-chip contact length (CCL). Nasr and Outeiro [19] conducted a sensitivity analysis of the CCL, cutting forces, and shear angle during dry and cryogenic orthogonal turning of AZ31B-O. The CCL showed a significant increase with an elevated feed rate which is corelated to the increase in cutting forces along the increasing feed rate. Zakaria et al. [20] additionally investigated CCL by examining the effects of submerged convective cooling (SCC) and varying machining parameters on the formation of BUL/BUE, cutting forces, and CCL in the orthogonal turning of AZ31 with a benchmarked dry cutting test. Elevated chip contact lengths and cutting forces were noted at increased cutting speeds in the dry cutting test.

Nasr and Outeiro [19] investigated the chip compression ratio (CCR) and shear angle of the resultantly prevalent saw-tooth chips. The CCR increased with increasing feed rate and the shear angle decreased with the increasing feed rate. Fang et al. [21] investigated the limits of such a process by monitoring mean flank temperatures during the high-speed dry end-milling of AZ91. Flank face temperatures of over 250 °C were recorded during the machining process. If further increased, this could pose a large risk due to magnesium chip ignition. Viswanathan et al. [22] investigated and optimized the process parameters based on flank wear, surface roughness, cutting forces, and cutting temperatures during turning of AZ91D in dry and MQL conditions. The usage of MQL resulted in less flank wear and surface roughness, as compared to dry cutting. However, cutting forces increased during the usage of MQL, which is likely due to the minor mitigation of thermal softening. According to the conducted GRA, the cutting environment was the second most critical variable following the feed rate. The cut depth and cutting speed were ranked third and fourth, respectively. The optimum predicted and validated cutting condition was the highest cutting speed coupled with the lowest feed rate and cut depth under MQL

conditions. A similar study was conducted by Cagan et al. [23] exploring the effects of cutting parameters on tool wear, cutting forces, and chip morphology categorization during the turning of AZ91D in dry and MQL environments. The presence of adhered material, in the form of BUL/BUE, was noted on the tool in both cutting environments. However, the usage of MQL resulted in less cutting forces due to the lubrication effect of the cutting fluid.

MQL systems have not been utilized and tested thoroughly for magnesium alloy machining, as compared to other alloys. The use of more sustainable cutting fluids, such as vegetable oil-based cutting fluids (VCFs), has also yet to be prefaced for magnesium alloys. Vegetable esters are a possible replacement to conventional petroleum-based cutting fluids since they react with the surface of the machined metal and produce chlorides and sulphides which reduce tribological tool-workpiece/tool-chip friction mechanics and cutting temperatures [24]. The usage of vegetable oil-based cutting fluids has been assessed for other lightweight alloys, such as titanium and aluminium alloys and offered promising results [25]. The use of vegetable oil-based cutting fluids can result in improved tool life, surface quality, and cutting forces in comparison to conventional dry and petroleum-based flood cooling techniques in a multitude of ferrous and nonferrous alloys [26,27].

Akyuz [28] investigated the effect of aluminium content towards the wear resistance and machining performance for the AZ cast magnesium alloys. It was found that AZ91 provided the highest wear resistance. Whereas AZ21 was found with poor machinability. Kuczmaszewski et al. [29] focused his work to investigate the shape and fragmentation of chips when machining AZ91HP. The study indicated that less chip fragmentation was obtained when a rake angle of 30° was utilized in the study. Pradeepkumar et al. [30] utilized the concepts of response surface methodology, artificial neural network, and genetic algorithm to investigate the surface integrity of the machined component made out of magnesium alloy. The study found that RSM and ANN models provided 2.4% and 1.52% average error, respectively. Then, the ANN model was coupled with a genetic algorithm to obtain the optimized conditions for surface integrity. A brief summary of the literature review activity can be found in Table 1.

Chip morphology is an important indicator of machinability which can assess shearing forces and signify cutting energy and surface finish. However, due to the relative novelty of magnesium alloys, a thorough investigation of chip morphology parameters is yet to be found in the field of available literature. To further increase the machinability, as well as maintain sustainability, magnesium machinability has also been scarcely tested under minimum quantity lubrication (MQL) conditions. Additionally, since no thorough optimization/analysis of chip morphology parameters was found within the literature regarding the conventional or highspeed machining of magnesium alloys, this work intends to do just that. The present study aimed at the assessment and optimization of the machinability of AZ91 magnesium alloy in orthogonal turning, based on tool wear and chip morphology parameters in an MQL cutting environment using GRA and other statistical techniques.

Table 1. Literature review summary.

Source No.	Authors	Material	Topics of Interest along Scope of Investigation	Cutting Environment	Machining Parameters	Tool	Take-Away Conclusions
13	Viswanathan et al.	AZ91D	GRA, Cutting forces, Flank wear, Surface roughness, MRR	Dry	Turning Vc = 40–120 m/min f = 0.1–0.3 mm/rev DOC= 0.5–1 mm	PVD CNMG120408 insert	Cutting forces and flank wear increased with feed rate and cut depth. Surface roughness decreased at elevated cutting speeds and increased with increasing feed rate and cut depth.
14	Shi et al.	AZ91D	Cutting forces, Surface roughness, Chip morphology	Dry	End-milling Vc = 50–400 m/min f = 0.4–0.8 mm/rev DOC = 1.5 mm	Uncoated 390-11T304E-NLH13A insert	Cutting forces decreased at increasing cutting speeds and increased at increasing feed rate. Surface roughness increased with increasing cutting parameters. Elevated feed rate resulted in loose saw-tooth chips.
15	Ramesh et al.	AZ91D	GRA, Surface roughess, Tool wear	Dry	Turning Vc = 40–120 m/min f = 0.1–0.2 mm/rev DOC = 0.5–1 mm	PCD SNMG120404	Increased in any cutting parameter. Increased tool wear and surface roughness. Feed rate, Cutting speed, and depth of cut ranked as influencing parameters 1,2, and 3 respectively.
16	Tönshoff & Winkler	AZ9AHP	BUL/BUE, Cutting forces, Surface roughness	Dry	Turning Vc = 900 m/min f = 0.4 mm/rev DOC = 1.5 mm	HW, HC, PCD CCMW 120408 CCMT 120408	Increased BUL/BUE noted on TiN tool. Cutting forces elevated due to BUL/BUE. Surface quality hindered by presence of adhered material.

Table 1. *Cont.*

Source No.	Authors	Material	Topics of Interest along Scope of Investigation	Cutting Environment	Machining Parameters	Tool	Take-Away Conclusions
17	J. Wang et al.	AZ91	Tool wear	Dry	Drilling Vc = 1000–8000 rpm f = 0.05–0.3 mm/rev	Uncoated HSS drill tool	Majority of the wear map dominated by adhesive wear with area at the centre of the map identified with excessive BUE.
18	Carou et al.		Magnesium alloys machinability review				Main mechanism of tool wear progression is adhesion,
19	Nasr & Outeiro	AZ31B-O	CCL, CCR, Cutting forces, Shear angle	Dry, Cryogenic	Orthogonal turning Vc = 100 m/min f = 0.1 & 0.2 mm/rev DOC = 3 mm	Uncoated carbide insert	CCL and cutting forces increased with increasing feed rate.
20	Zakaria et al.	AZ31	BUL/BUE, Cutting forces, CCL	Dry, SCC	Orthogonal turning Vc = 120–240 m/min f = 0.2 mm/rev DOC = 1 mm	Uncoated CNMA120408 insert	Cutting forces and CCL increased at increased cutting speeds. Increased friction at tool-chip interface results in increased melting and adhesion of chips as well as elevated forces.
21	Fang et al.	AZ91	Mean flank temperatures	Dry	End-milling Vc = 408–1088 m/min f = 50–7000 mm/min DOC = 0.05–3 mm	Tungsten carbide ball-nose end mills	Flank temperatures exceeded 250 °C which could pose possible chip ignition risks.
22	Viswanathan et al.	AZ91D	GRA, Flank wear, Surface roughness, Cutting forces, Cutting temperatures	Dry/MQL	Turning Vc = 40–140 m/min f = 0.1–0.3 mm/min DOC = 0.5–1 mm	Uncoated CNMG 120408 insert	MQL resulted in less flank wear, surface roughness, and cutting temperatures. Increased cutting forces noted under MQL. Cutting environment is the second most critical variable after feed rate.

Table 1. *Cont.*

Source No.	Authors	Material	Topics of Interest along Scope of Investigation	Cutting Environment	Machining Parameters	Tool	Take-Away Conclusions
23	Cagan et al.	AZ91D	Tool wear, Cutting forces, Chip morphology	Dry/MQL	Turning Vc = 500–1000 m/min f = 0.05–0.2 mm/min DOC = 0.5–1.5 mm	CCGT, DCGT, VCGT	FBU noted in all cutting parameters and environments. MQL resulted in reduced cutting forces. Cut depth found to be most critical parameter and cutting environment to be least critical.
28	Akyuz	AZ01, AZ21, AZ41, AZ61 and AZ91	Wear resistance and Cutting force	Dry	Feed rate (f) 0.10 mm/rev, DoC 0.5 mm, Cutting speed (Vc) 56, 112, 168 m/min	CCGT 120408 FL K10	It was found that AZ91 provided the highest wear resistance. Whereas AZ 21 was found with poor machinability.
29	Kuczmaszewski et al.	AZ91 HP	Chip fragmentation	Dry	Cutting speed 400–800 m/min, Feed rate 0.15–0.3 mm/tooth	16 mm carbide end mill	The study provided that less chip fragmentation was obtained when rake angle of 30° was utilized in the study.
30	Pradeepkumar et al.	AZ91D	Surface roughness	Dry	Spindle rev 750–1000 rpm, Feed 75–100 rev/min	End milling cutter	The study found that RSM and ANN models provided 2.4% and 1.52% average error, respectively.

2. Materials and Methods

2.1. Tool and Material Information

Extruded AZ91 rods were conventionally machined into workpieces with discs of 1.5 mm thickness and 50 mm diameter in preparation for orthogonal turning, as seen in Figure 1a. Table 2 shows the chemical composition and mechanical properties of AZ91. Titanium nitride (TiN) coated TNMG160404-TN2000 CVD cutting inserts, as shown in Figure 1b, and manufactured by Widia were utilized and clamped into the Dormer Pramet PTGNR 2020 K16 tool holder.

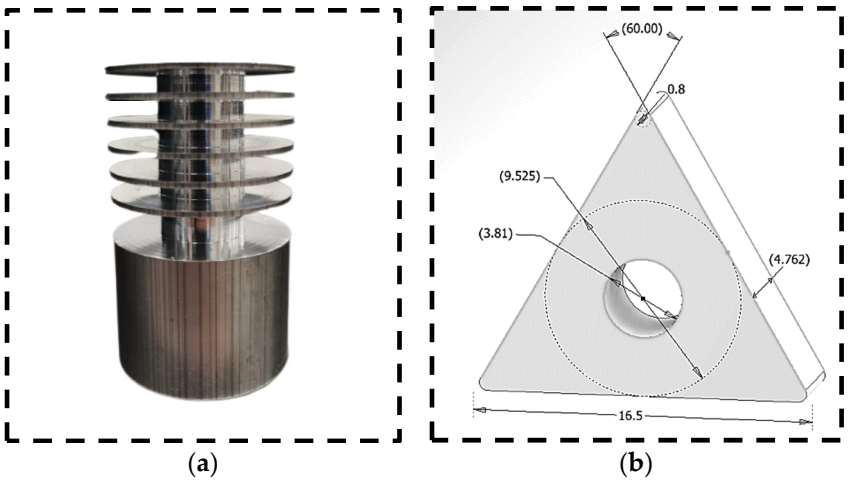

Figure 1. (**a**) AZ91 workpiece specimen prepared for orthogonal cutting; (**b**) geometry in millimetre of the cutting insert.

Table 2. Chemical composition and mechanical properties of AZ91 at room temperature [31,32].

	Element Content, wt%							
AZ91	Al	Zn	Mn	Si	Ni	Cu	Fe	Mg
	8.3~9.7	0.35~1.0	0.15~0.5	0.1	0.002	0.03	0.005	Balance
	Ultimate strength		Hardness	Elongation		Poisson's Ratio		Density
	172 MPa		59 HB	3.4%		0.35		1.78 g/cm^3

2.2. Machining Set-Up

The cutting tests conducted on a Jyoti DX 135 nvu CNC turning centre invoked the usage of ECULUBRIC E200L, a vegetable oil-based natural glyceride cutting fluid at room temperature. The measurement of tool wear, chip-tool contact length, and chip morphology was performed using an optical microscope (Model: SWT350T, Swift Optical Instruments, Inc., Schertz, TX, USA), as shown in Figure 2. Figure 2 shows the pictorial illustration of the measurements of the chip morphology, tool wear, and contact length. The optical microscope has a double-layered mechanical stage with a slide holder, stage size of 130 mm × 130 mm, and stage X-Y range of 70 mm × 30 mm. The said cutting fluid has a flash point and ignition point of 325 °C and 365 °C, respectively, as well as a density, viscosity, and partition coefficient of 0.92 g/cm^3, 70 cP, and <3%, respectively. A UNIST SPR-2000-3GALLV MQL system tank containing the cutting fluid was pressurized to 2 bars and connected to the spray nozzle, as seen in Figure 3a. The variable flow rate spray nozzle was located at 12 mm above the cutting zone, and supplied a mist of air and cutting fluid directly into the tool-workpiece/tool-chip interface, as seen in Figure 3b.

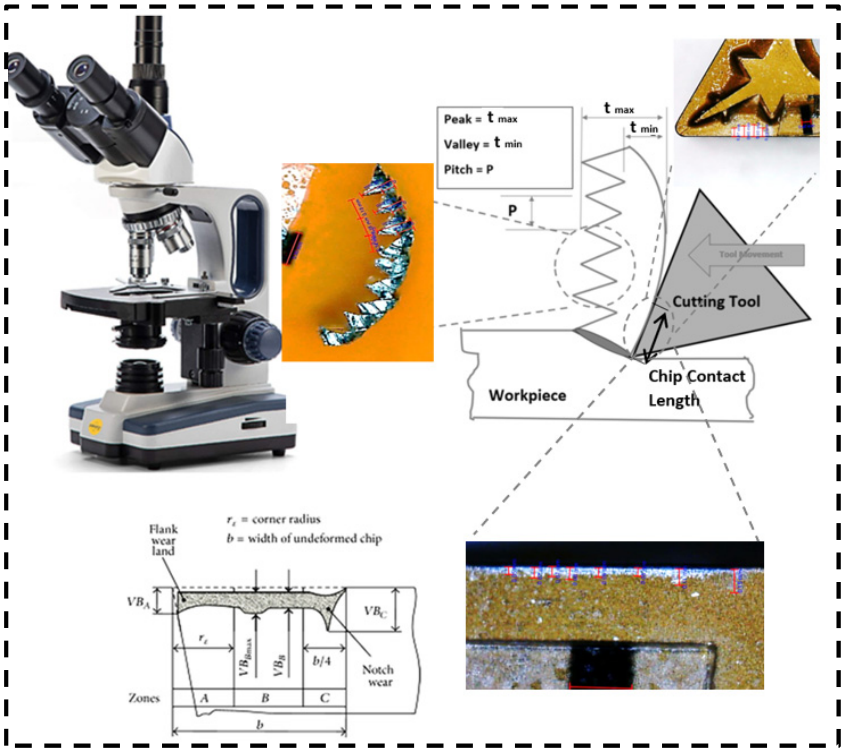

Figure 2. Pictorial illustration of the optical Swift microscope SWT350T used for the measurement of the chips, tool wear, and chip-tool contact length.

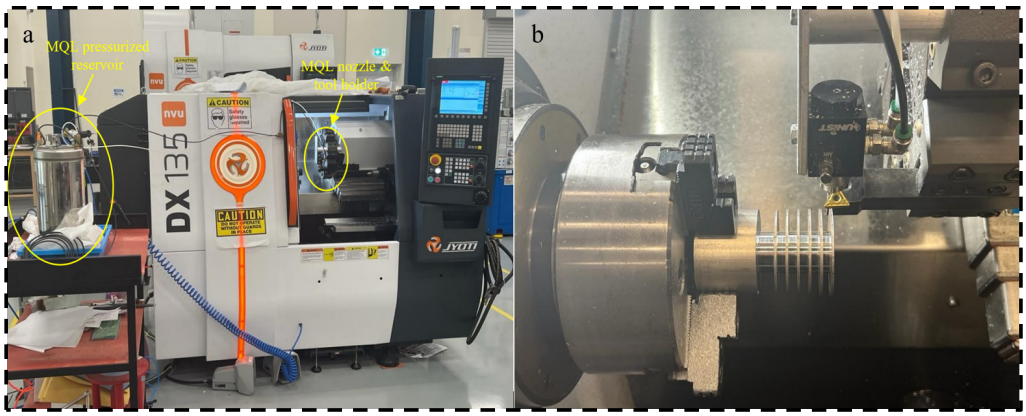

Figure 3. (**a**) CNC lathe and MQL setup; (**b**) cutting setup.

2.3. Full Factorial Experimental Design

The control parameters chosen for this full factorial experimentation were the cutting fluid flow rate, cutting speed (Vc), and feed rate (f) at a constant depth of cut (DOC) of 1.5 mm. The magnitudes of each level along with the parameter letter designation, in preparation for GRA, can be seen in Table 3. The full factorial design was computed by number of experiments = Xˆk, where X is the number of levels, and k is the number of variables for the factors. So, in our case, it was $3 \times 3 = 27$ experiments and with two replications, the total experiments were 54. The Minitab program was utilized to formulate the final full factorial experimental procedure table presented in Table 4. Each experimental trial was conducted using a constant radial machining length of 10mm, which meant the machining of an entire disc. Following an experimental trial, the chips were collected and inspected for morphology and the utilized tool's rake and flank face were examined for chip contact length and flank wear. The cutting tool was oriented to a fresh cutting edge or replaced prior to every experimental trial. For the sake of precision, the tests entailed a

replication value of 2, which meant that every experiment was conducted twice under the same cutting conditions.

Table 3. Experimental design.

Levels	MQL Flow Rate (mL/h) A	Cutting Speed (m/min) B	Feed (mm/rev) C
3	120	300	0.5
2	80	250	0.4
1	40	200	0.3

Table 4. Experimental input and output raw responses.

Exp No.	A: MQL (mL/h)	B: Vc (m/min)	C: f (mm/rev)	Vb (mm)	CCL (mm)	P (mm)	CR (mm)	SR (mm)	φ (rad)
1	120	200	0.5	0.203	0.695	0.447	0.727	0.594	0.942
2	120	200	0.3	0.071	0.298	0.117	0.628	0.493	1.010
3	120	200	0.4	0.081	0.423	0.380	0.658	0.577	0.989
4	120	250	0.3	0.081	0.388	0.173	0.883	0.500	0.847
5	120	250	0.4	0.099	0.563	0.237	0.804	0.538	0.894
6	120	250	0.5	0.136	0.723	0.473	0.690	0.629	0.967
7	120	300	0.3	0.056	0.423	0.157	0.794	0.479	0.899
8	120	300	0.5	0.138	0.855	0.477	0.713	0.601	0.951
9	120	300	0.4	0.086	0.745	0.463	0.746	0.568	0.930
10	80	200	0.4	0.058	0.678	0.247	0.733	0.533	0.938
11	80	200	0.5	0.123	0.815	0.373	0.750	0.558	0.927
12	80	200	0.3	0.185	0.378	0.157	0.811	0.525	0.889
13	80	250	0.5	0.124	0.810	0.527	0.690	0.478	0.967
14	80	250	0.3	0.081	0.568	0.150	0.467	0.645	1.134
15	80	250	0.4	0.080	0.488	0.327	0.658	0.509	0.989
16	80	300	0.5	0.100	0.780	0.373	0.580	0.574	1.045
17	80	300	0.3	0.055	0.438	0.240	0.506	0.662	1.103
18	80	300	0.4	0.104	0.638	0.380	0.692	0.544	0.966
19	40	200	0.5	0.186	0.783	0.417	0.557	0.495	1.063
20	40	200	0.3	0.080	0.420	0.160	0.606	0.566	1.026
21	40	200	0.4	0.093	0.603	0.490	0.604	0.645	1.027
22	40	250	0.5	0.096	0.833	0.553	0.670	0.543	0.980
23	40	250	0.4	0.076	0.533	0.463	0.479	0.663	1.124
24	40	250	0.3	0.063	0.550	0.217	0.778	0.511	0.910
25	40	300	0.5	0.083	0.725	0.423	0.607	0.589	1.025
26	40	300	0.4	0.070	0.573	0.440	0.525	0.701	1.087
27	40	300	0.3	0.063	0.423	0.283	0.528	0.681	1.085

Where MQL = minimum quantity lubrication, Vc = cutting speed, f = feed, Vb = flank tool wear, CCL = chip contact length, t max = peak distance, t min = valley distance, P = pitch distance, chip segmentation ratio (SR), compression ratio = CR and shear angle (φ).

3. Results and Discussion

3.1. Data Processing and Parameter Computation

Average flank wear measurements were conducted following every experimental trial, as presented in Figure 4a. The presence of BUL/BUE was noted on all measurement images following every experimental trial, signifying the prevalence of adhesion as the predominant mechanism of flank wear evolution. The rake face was also inspected for chip contact length (CCL) following every experimental trial, as seen in Figure 4b. The average readings of the flank wear land width (Vb) and CCL per experimental trial were considered for further analysis.

The chips collected all presented exaggerated saw-tooth characteristics with the majority being fragmented into short length segments. The nature of these damaged/loose saw-tooth chips indicates the intense shearing and plastic deformation that occurred due to aggressive cutting parameters. Moreover, the chips collected were inspected for saw-tooth morphology parameters following each experimental trial, as seen in Figure 5a. Three saw-tooth segments were measured for tooth peak height (t max), valley height (t min), and pitch (P), as portrayed in Figure 5b, and the mean value of each was considered for further analysis. The tool wear and chip morphology data along with their corresponding input parameters are presented in Table 5.

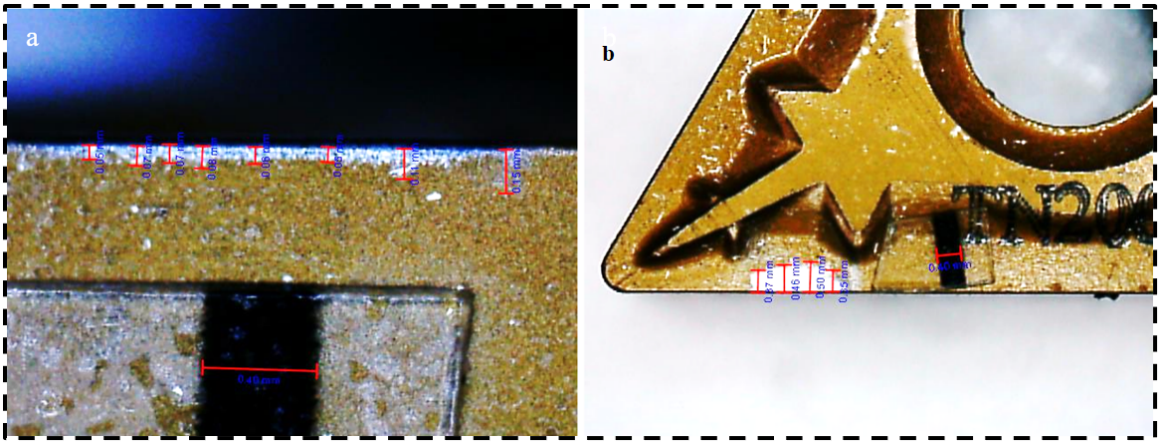

Figure 4. 20th Experimental trial; (**a**) flank wear land width; (**b**) chip contact length.

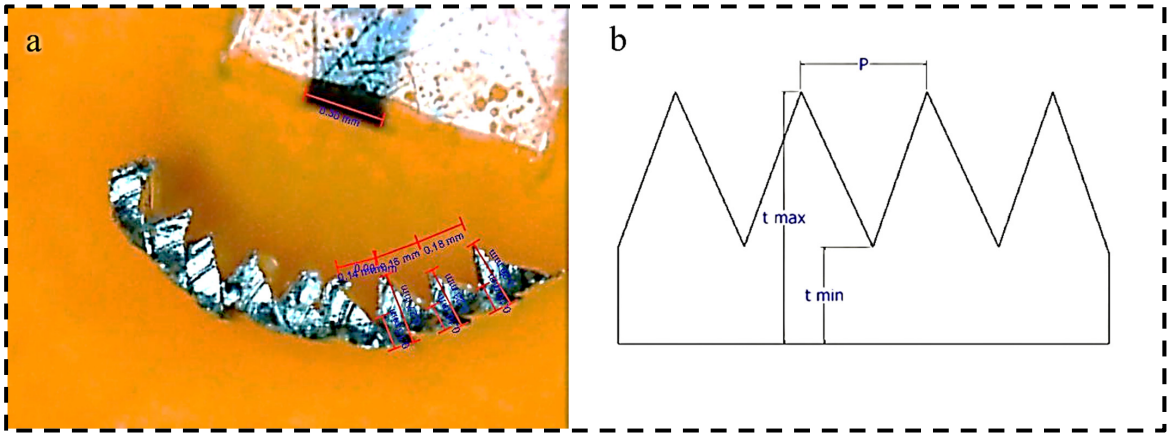

Figure 5. (**a**) 20th Experimental trial chip measurements; (**b**) illustration of the parameter measurements.

Chip morphology parameters, such as chip compression ratio, chip segmentation ratio, and shear angle are crucial to determining the degree of plastic deformation occurring due to the selected cutting parameters. The chip compression ratio parameter is an indicator of the interplay between the thermal softening and strain hardening phenomena that occur within the chip formation process. Further, the shear angle is a key parameter by which many of the remaining desired parameters can be computed through. Due to the presence of saw-tooth chips, the computation of the chip compression ratio (CR) was conducted, as presented in [33], by which an average value of chip thickness is utilized to compute the chip compression ratio, as presented in Equation (1).

$$CR = \frac{t_{max} + t_{min}}{2f} \tag{1}$$

Further, the computation of the chip segmentation ratio (SR) and shear angle (φ) were conducted, as per the experimental investigation of Pervaiz et al. [34]. In the presence of a saw-tooth chip, the segmentation ratio (SR) is considered as the ratio of peak and valley differences to the peak height, as presented in Equation (2). Moreover, the shear angle (φ) was computed through the rake angle (γ), as shown in Equation (3).

$$SR = \frac{t_{max} - t_{min}}{t_{max}} \tag{2}$$

$$\varphi = \tan^{-1}\left(\frac{\cos\gamma}{CR - \sin\gamma}\right) \tag{3}$$

Table 5. GRA step 1: letter designation and output data.

Exp. No	A	B	C	Vb (mm)	CCL (mm)	P (mm)	CR (mm)	SR (mm)	φ (rad)
1	3	1	3	0.203	0.695	0.447	0.727	0.594	0.942
2	3	1	1	0.071	0.298	0.117	0.628	0.493	1.010
3	3	1	2	0.081	0.423	0.380	0.658	0.577	0.989
4	3	2	1	0.081	0.388	0.173	0.883	0.500	0.847
5	3	2	2	0.099	0.563	0.237	0.804	0.538	0.894
6	3	2	3	0.136	0.723	0.473	0.690	0.629	0.967
7	3	3	1	0.056	0.423	0.157	0.794	0.479	0.899
8	3	3	3	0.138	0.855	0.477	0.713	0.601	0.951
9	3	3	2	0.086	0.745	0.463	0.746	0.568	0.930
10	2	1	2	0.058	0.678	0.247	0.733	0.533	0.938
11	2	1	3	0.123	0.815	0.373	0.750	0.558	0.927
12	2	1	1	0.185	0.378	0.157	0.811	0.525	0.889
13	2	2	3	0.124	0.810	0.527	0.690	0.478	0.967
14	2	2	1	0.081	0.568	0.150	0.467	0.645	1.134
15	2	2	2	0.080	0.488	0.327	0.658	0.509	0.989
16	2	3	3	0.100	0.780	0.373	0.580	0.574	1.045
17	2	3	1	0.055	0.438	0.240	0.506	0.662	1.103
18	2	3	2	0.104	0.638	0.380	0.692	0.544	0.966
19	1	1	3	0.186	0.783	0.417	0.557	0.495	1.063
20	1	1	1	0.080	0.420	0.160	0.606	0.566	1.026
21	1	1	2	0.093	0.603	0.490	0.604	0.645	1.027
22	1	2	3	0.096	0.833	0.553	0.670	0.543	0.980
23	1	2	2	0.076	0.533	0.463	0.479	0.663	1.124
24	1	2	1	0.063	0.550	0.217	0.778	0.511	0.910
25	1	3	3	0.083	0.725	0.423	0.607	0.589	1.025
26	1	3	2	0.070	0.573	0.440	0.525	0.701	1.087
27	1	3	1	0.063	0.423	0.283	0.528	0.681	1.085

Equations (1)–(3) were used to compute the chip morphology parameters for all experimental trials and the final list of input and output parameters is presented in Table 4. In the machining of aluminium, titanium, and even steel alloys, the compression ratio is usually greater than 1 [35–39]. However, during the machining of light weight alloys at speeds that are relatively high in comparison to their conventional ranges, largely elevated cutting temperatures coupled with the material's higher toughness results in occurrences where the chip compression ratio is less than 1 [40]. A trend of decreasing chip compression ratio can be seen in the increasing feed rate and cutting speed, as well as in the decreasing rake angle during the machining of aluminium alloys and metal matrix composites (MMCs), as seen by [41–43].

3.2. Full Factorial Design Based Data Analysis

As shown in Figure 6, normal probability charts of the output response data have been plotted. A normal probability chart is a popular graphical representation of the normal distribution of data. If the data points roughly form the straight line, then one can suggest that data is normally distributed. The normality of the data, as observed in this case, exhibits that it can be processed with statistical techniques in order to obtain reliable results.

The behaviour of each response was also obtained using the model of fit, as shown in Equations (4)–(8). To simplify the model equations for each output responses, only the first term interactions are considered. In the mentioned equations, the positive and negative values of coefficients have certain meaning. The positive value indicates that the output variable will increase with the associated increasing input variable. Moreover, the negative

coefficients mean that the output variables will decrease with the associated decreasing input variables.

$$Vb = 0.09893 - 0.00893\ A_1 + 0.00219\ A_2 + 0.00674\ A_3 + 0.02107\ B_1 - 0.00604\ B_2 - 0.01504\ B_3 - 0.01726\ C_1 - 0.01593\ C_2 + 0.03319\ C_3 \quad (4)$$

$$CCL = 0.5981 + 0.0067\ A_1 + 0.0233\ A_2 - 0.0300\ A_3 - 0.0322\ B_1 + 0.0081\ B_2 + 0.0241\ B_3 - 0.1663\ C_1 - 0.0154\ C_2 + 0.1818\ C_3 \quad (5)$$

$$CR = 0.6624 - 0.0675\ A_1 - 0.0083\ A_2 + 0.0757\ A_3 + 0.0125\ B_1 + 0.0175\ B_2 - 0.0300\ B_3 + 0.0311\ C_1 - 0.0537\ C_2 + 0.0226\ C_3$$

$$P = 0.3387 + 0.0442\ A_1 - 0.0304\ A_2 - 0.0138\ A_3 - 0.0289\ B_1 + 0.0080\ B_2 + 0.0209\ B_3 - 0.1549\ C_1 + 0.0421\ C_2 + 0.1128\ C_3 \quad (6)$$

$$SR = 0.5704 + 0.0289\ A_1 - 0.0117\ A_2 - 0.0172\ A_3 - 0.0164\ B_1 - 0.0131\ B_2 + 0.0295\ B_3 - 0.0387\ C_1 + 0.0326\ C_2 + 0.0061\ C_3 \quad (7)$$

$$\varphi = 0.9894 + 0.0469\ A_1 + 0.0059\ A_2 - 0.0529\ A_3 - 0.0104\ B_1 - 0.0103\ B_2 + 0.0207\ B_3 - 0.0221\ C_1 + 0.0390\ C_2 - 0.0170\ C_3 \quad (8)$$

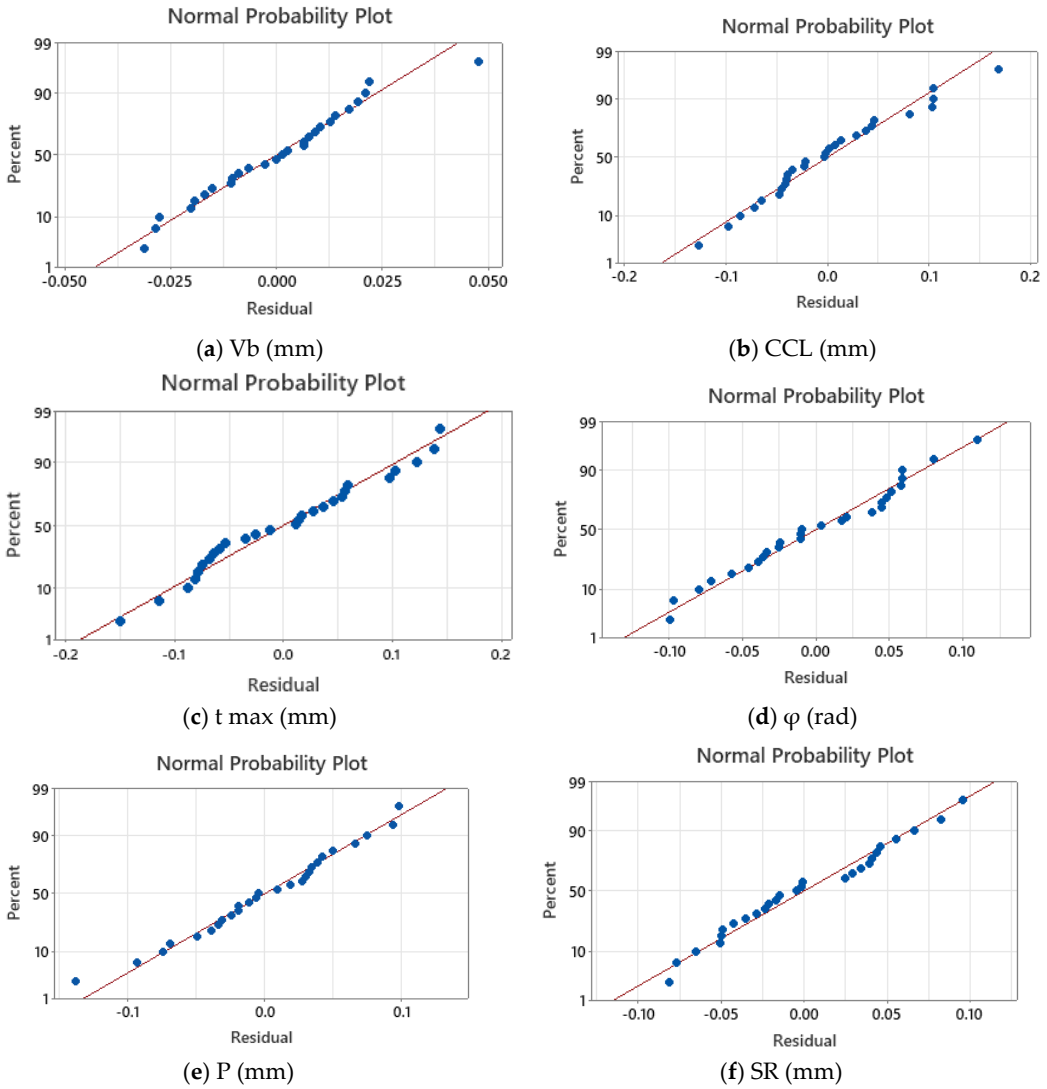

(**a**) Vb (mm) (**b**) CCL (mm)

(**c**) t max (mm) (**d**) φ (rad)

(**e**) P (mm) (**f**) SR (mm)

Figure 6. Normal probability plots for the output responses.

A Pareto diagram is a tool that is used to help in the identification of the significance of factors towards their contribution on the output responses. Standardized effects show the size of the effect relative to the total variation in the data. This diagram is used in the full factorial analysis to figure out the focused areas for improvement. There is a reference line on the diagram that represents a critical value (2.086 in Figure 7a), if the effect is more than this value, then it is considered as significant. Figure 7a–f show that feed was found to be a significant parameter for flank wear, chip contact length, pitch values, and segmentation ratio. The MQL flow rate and feed were found to be significant for the peak and valley values of the chips. For the shear angle, the MQL flow rate was found to be the most dominant parameter.

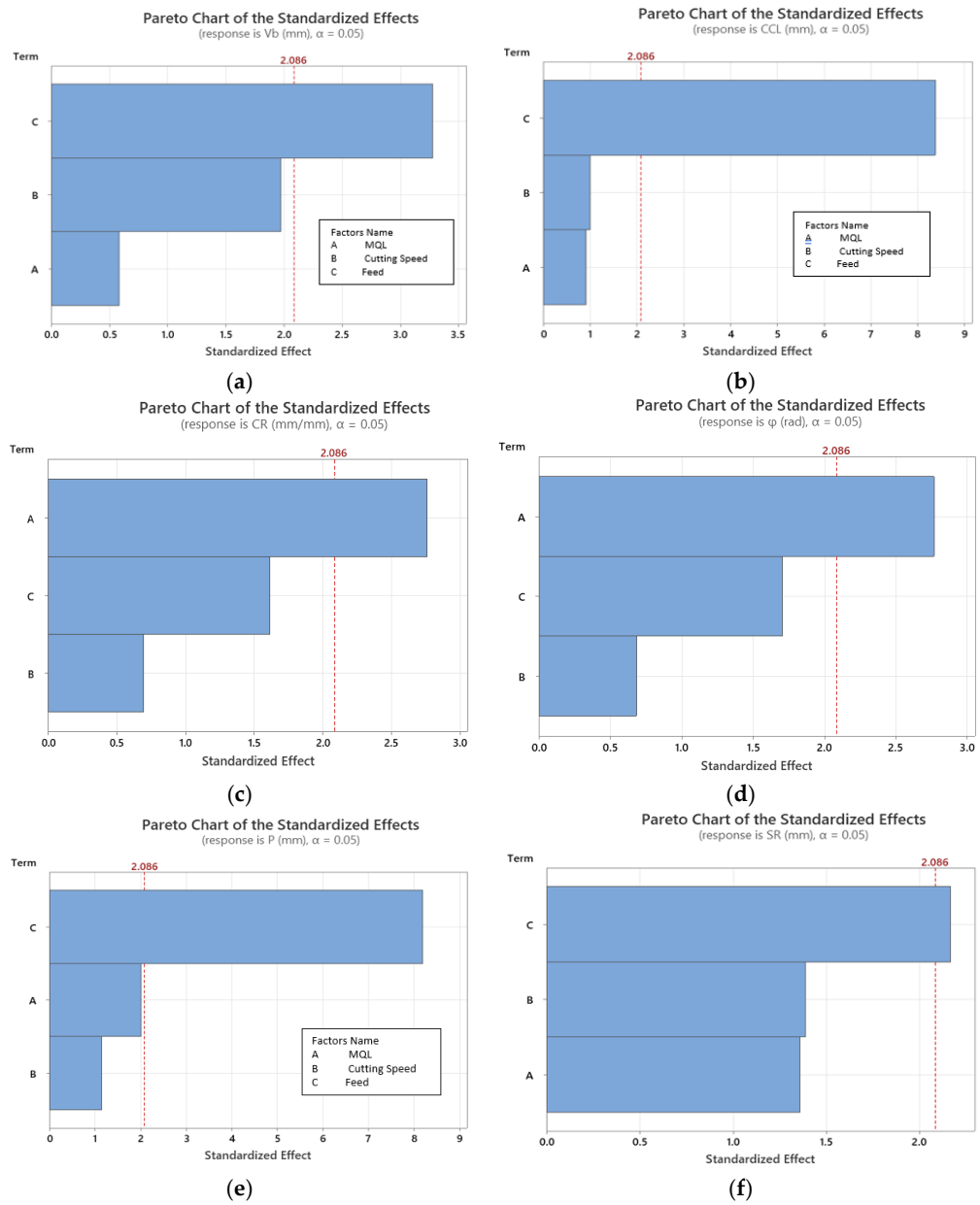

Figure 7. Pareto chart of the standardized effects.

3.3. Grey Relational Analysis

The use of a grey relational analysis was invoked due to its highly reputable capabilities for determining optimal parameters in complicated multi-variant problems [44]. Input and output response lists are generated and presented in Table 5, following the letter designation of the input parameters presented in Table 3.

The data are then normalised, which allow each output response to be scaled down to a value between 0 and 1 in reference to each parameter's own range of data [45]. This is achieved through initially determining which parameters would ideally be maximized or minimized. In the current case, all output responses would optimally be minimized except for the shear angle (φ), since a lower shear angle would indicate larger ratios of segmentation. As presented by Jozić et al. [46], the manner to achieve the normalisation of parameters that are optimally minimized (smaller-the-better) is presented through the ratio of the difference between the maximum value ($\max(y_{ij})$) within a response range and the current value (y_{ij}) to the difference between the maximum and minimum ($\min(y_{ij})$) values in the selected range, as presented in Equation (9).

$$x_{ij} = \frac{\max(y_{ij}) - y_{ij}}{\max(y_{ij}) - \min(y_{ij})} \quad (9)$$

A similar relation is mentioned by Jozić et al. [46] regarding the normalisation of optimally maximized (larger-the-better) parameters. The relation is presented as the ratio of the difference of the current value (y_{ij}) and the minimum value within the response range ($\min(y_{ij})$) to the difference of the maximum ($\max(y_{ij})$) and minimum ($\min(y_{ij})$) values within the response range, as shown in Equation (10).

$$x_{ij} = \frac{y_{ij} - \min(y_{ij})}{\max(y_{ij}) - \min(y_{ij})} \quad (10)$$

The normalised output responses are presented in Table 6.

Table 6. GRA step 2: normalised output responses.

Vb (mm)	CCL (mm)	P (mm)	CR (mm)	SR (mm)	φ (rad)
0	0.28725314	0.75688073	0.375	0.520179372	0.33101
0.89189189	1	0	0.61298077	0.067264574	0.567944
0.82432432	0.77558348	0.60321101	0.54086538	0.443946188	0.494774
0.82432432	0.83842011	0.12844037	0	0.098654709	0
0.7027027	0.52423698	0.27522936	0.18990385	0.269058296	0.163763
0.4527027	0.23698384	0.81651376	0.46394231	0.677130045	0.418118
0.99324324	0.77558348	0.09174312	0.21394231	0.004484305	0.181185
0.43918919	0	0.82568807	0.40865385	0.551569507	0.362369
0.79054054	0.19748654	0.79357798	0.32932692	0.403587444	0.289199
0.97972973	0.31777379	0.29816514	0.36057692	0.246636771	0.317073
0.54054054	0.07181329	0.58715596	0.31971154	0.358744395	0.278746
0.12162162	0.85637343	0.09174312	0.17307692	0.210762332	0.146341
0.53378378	0.08078995	0.94036697	0.46394231	0	0.418118
0.82432432	0.51526032	0.07568807	1	0.748878924	1
0.83108108	0.65888689	0.48165138	0.54086538	0.139013453	0.494774
0.69594595	0.13464991	0.58715596	0.72836538	0.430493274	0.689895
1	0.7486535	0.28211009	0.90625	0.825112108	0.891986
0.66891892	0.38958707	0.60321101	0.45913462	0.295964126	0.414634
0.11486486	0.12926391	0.68807339	0.78365385	0.076233184	0.752613
0.83108108	0.78096948	0.09862385	0.66586538	0.394618834	0.623693
0.74324324	0.4524237	0.85550459	0.67067308	0.748878924	0.627178
0.72297297	0.03949731	1	0.51201923	0.291479821	0.463415
0.85810811	0.57809695	0.79357798	0.97115385	0.829596413	0.965157
0.94594595	0.5475763	0.2293578	0.25240385	0.147982063	0.219512
0.81081081	0.23339318	0.70183486	0.66346154	0.497757848	0.620209
0.89864865	0.50628366	0.74082569	0.86057692	1	0.836237
0.94594595	0.77558348	0.38073394	0.85336538	0.910313901	0.829268

Next, the standard deviation Δx_{ij} is computed through finding the deviation of the current response y_{ij} from the ideal reference case y_{0j}, which corresponds to a value of 1, as shown in Equation (11). The deviation sequence list is presented in Table 7.

$$\Delta x_{ij} = y_{ij} - y_{0j} \tag{11}$$

Table 7. GRA step 3: deviation sequence.

Vb (mm)	CCL (mm)	P (mm)	CR (mm)	SR (mm)	φ (rad)
1	0.712747	0.243119	0.625	0.479821	0.66899
0.1081081	0	1	0.387019	0.932735	0.432056
0.1756757	0.224417	0.396789	0.459135	0.556054	0.505226
0.1756757	0.16158	0.87156	1	0.901345	1
0.2972973	0.475763	0.724771	0.810096	0.730942	0.836237
0.5472973	0.763016	0.183486	0.536058	0.32287	0.581882
0.0067568	0.224417	0.908257	0.786058	0.995516	0.818815
0.5608108	1	0.174312	0.591346	0.44843	0.637631
0.2094595	0.802513	0.206422	0.670673	0.596413	0.710801
0.0202703	0.682226	0.701835	0.639423	0.753363	0.682927
0.4594595	0.928187	0.412844	0.680288	0.641256	0.721254
0.8783784	0.143627	0.908257	0.826923	0.789238	0.853659
0.4662162	0.91921	0.059633	0.536058	1	0.581882
0.1756757	0.48474	0.924312	0	0.251121	0
0.1689189	0.341113	0.518349	0.459135	0.860987	0.505226
0.3040541	0.86535	0.412844	0.271635	0.569507	0.310105
0	0.251346	0.71789	0.09375	0.174888	0.108014
0.3310811	0.610413	0.396789	0.540865	0.704036	0.585366
0.8851351	0.870736	0.311927	0.216346	0.923767	0.247387
0.1689189	0.219031	0.901376	0.334135	0.605381	0.376307
0.2567568	0.547576	0.144495	0.329327	0.251121	0.372822
0.277027	0.960503	0	0.487981	0.70852	0.536585
0.1418919	0.421903	0.206422	0.028846	0.170404	0.034843
0.0540541	0.452424	0.770642	0.747596	0.852018	0.780488
0.1891892	0.766607	0.298165	0.336538	0.502242	0.379791
0.1013514	0.493716	0.259174	0.139423	0	0.163763
0.0540541	0.224417	0.619266	0.146635	0.089686	0.170732

The grey relational coefficient GRC represents the difference between the regarded optimal value and the current value. This is presented as the ratio of the difference of minimum deviation Δ_{min} and the product of the maximum deviation Δ_{max} and the distinguishing coefficient ξ, taken as 0.5 as per [46], to the sum of the standard deviation Δx_{ij} and the product of ξ and Δ_{max}, as presented in Equation (12).

$$GRC_{ij} = \frac{\Delta_{min} - \xi\Delta_{max}}{\Delta x_{ij} + \xi\Delta_{max}} \tag{12}$$

Finally, the grey relational grade GRG is computed as the average GRC of all output responses along a single experimental trial, as seen in Equation (13). This allows for the comparative ranking of the experimental input parameters on the basis of a unified scale grade output response, with 1 being the best and 0 the worst. The GRG along with the corresponding input parameters and their ranking is presented in Table 8. It is noted that the highest MQL flow rate along with the lowest cutting speed and feed rate resulted in the most optimized output responses.

$$GRG_i = \frac{1}{n}\sum_{i=1}^{n} GRC_i \tag{13}$$

Table 8. GRA step 4: GRC sequence.

Exp. No	A	B	C	Vb (mm)	CCL (mm)	P (mm)	CR (mm)	SR (mm)	φ (rad)	GRG	Rank
1	3	1	3	0.333333	0.412287	0.67284	0.444444	0.510297	0.42772	0.46682	24
2	3	1	1	0.822222	1	0.333333	0.563686	0.348983	0.536449	0.600779	7
3	3	1	2	0.74	0.690211	0.557545	0.521303	0.473461	0.4974	0.579987	8
4	3	2	1	0.74	0.755767	0.364548	0.333333	0.3568	0.333333	0.48063	23
5	3	2	2	0.627119	0.51242	0.40824	0.381651	0.406193	0.374185	0.451635	25
6	3	2	3	0.477419	0.395878	0.731544	0.482599	0.607629	0.462158	0.526204	14
7	3	3	1	0.986667	0.690211	0.355049	0.388785	0.334333	0.379128	0.522362	15
8	3	3	3	0.471338	0.333333	0.741497	0.45815	0.527187	0.43951	0.495169	21
9	3	3	2	0.704762	0.383873	0.707792	0.427105	0.456033	0.41295	0.515419	16
10	2	1	2	0.961039	0.422931	0.416031	0.438819	0.398927	0.42268	0.510071	17
11	2	1	3	0.521127	0.350094	0.547739	0.423625	0.438114	0.409415	0.448352	26
12	2	1	1	0.362745	0.776848	0.355049	0.376812	0.387826	0.369369	0.438108	27
13	2	2	3	0.517483	0.352309	0.893443	0.482599	0.333333	0.462158	0.506887	19
14	2	2	1	0.74	0.507748	0.351047	1	0.665672	1	0.710744	5
15	2	2	2	0.747475	0.59445	0.490991	0.521303	0.367381	0.4974	0.5365	13
16	2	3	3	0.621849	0.366206	0.547739	0.647975	0.467505	0.617204	0.544746	12
17	2	3	1	1	0.665472	0.410546	0.842105	0.740864	0.82235	0.746889	3
18	2	3	2	0.601626	0.450283	0.557545	0.48037	0.41527	0.460674	0.494295	22
19	1	1	3	0.360976	0.364768	0.615819	0.697987	0.351181	0.668998	0.509955	18
20	1	1	1	0.747475	0.695381	0.356792	0.599424	0.452333	0.570577	0.57033	9
21	1	1	2	0.660714	0.477292	0.775801	0.602899	0.665672	0.572854	0.625872	6
22	1	2	3	0.643478	0.342348	1	0.506083	0.413729	0.482353	0.564665	11
23	1	2	2	0.778947	0.542356	0.707792	0.945455	0.745819	0.934853	0.775871	1
24	1	2	1	0.902439	0.524976	0.393502	0.400771	0.369818	0.390476	0.496997	20
25	1	3	3	0.72549	0.394755	0.626437	0.597701	0.498881	0.568317	0.568597	10
26	1	3	2	0.831461	0.503162	0.65861	0.781955	1	0.753281	0.754745	2
27	1	3	1	0.902439	0.690211	0.446721	0.773234	0.847909	0.745455	0.734328	4

Utilizing the Minitab program, the mean responses table has been generated, as presented in Table 9. Using the mean response table, Figure 8 has been constructed. According to the maximum mean response values for each cutting parameter level, the optimal cutting parameters were A1B3C1, which correlates to MQL = 40 mL/h, Vc = 300 m/min, and f = 0.3 mm/rev. The grade for the first experimental run conducted, A3B1C3, was taken as reference. Since a full factorial experimentation was conducted, a confirmation experiment is not necessary, since the experimental parameter combination is already present within the dataset. In comparison to the reference parameter combination, the predicted parameter experimental results show a 34.42% improvement in the results, as presented in Table 10.

Table 9. Mean output response table.

Response Table for Means			
Level	**A**	**B**	**C**
1	0.622373	0.527808	0.589019
2	0.54851	0.561126	0.58271
3	0.515445	0.597394	0.5146
Delta	0.106928	0.069586	0.074419
Rank	1	3	2
Average		0.56211	

Table 10. Prediction and confirmation of the parameter combination.

	Parameter Combination	**Grade**
Reference parameter combination	A3 B1 C3	0.46682
Optimal parameter combination available in the experimentation	A1 B3 C1	0.73432
	GRG improvement	0.2675

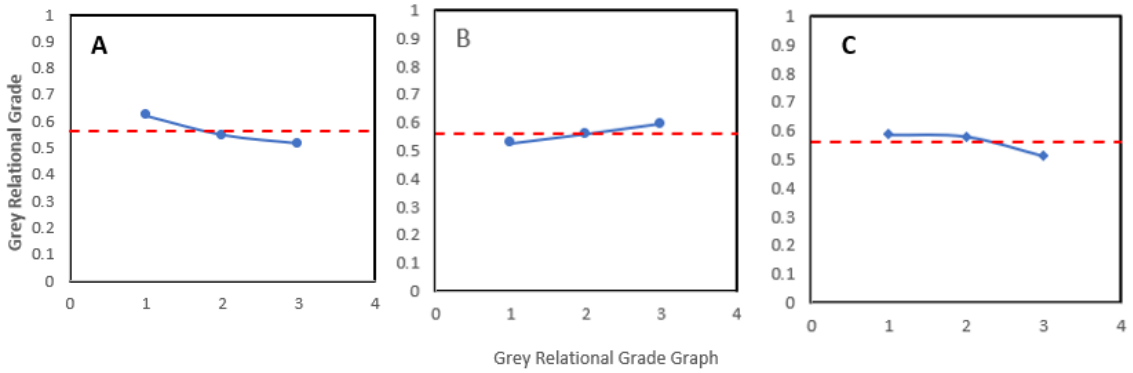

Figure 8. Grey relational grade graph.

The mean output response data in Table 10 was used to plot the mean response graph presented in Figure 9. The Minitab program was additionally utilized to present the analysis of variance (ANOVA), with a 95% confidence level, to reveal the percentage contribution of the individual parameters and their interaction on the grey relational grade (GRG), as presented in Table 11. As per the data presented, the largest individual contributing variable was the MQL flow rate (20%), followed by the cutting speed (8.9%), and the feed rate (5.59%) was deemed as the least critical variable.

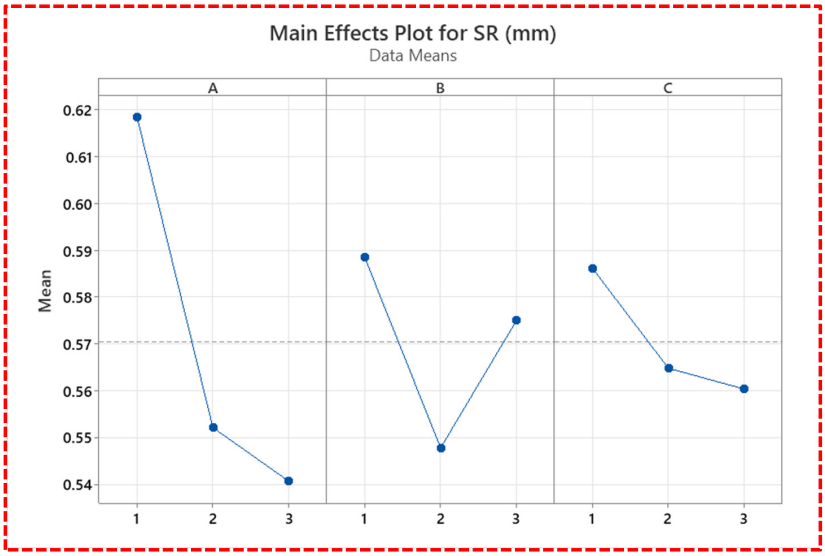

Figure 9. Main effects plot for the segmentation ratio.

Table 11. Analysis of variance (ANOVA) of the GRG.

Source	DF	Seq SS	Contribution	Adj SS	Adj MS	F-Value	*p*-Value
A: MQL	2	0.04541	20.00%	0.048534	0.024267	8.62	0.035
B: Cutting Speed	2	0.02021	8.90%	0.006475	0.003238	1.15	0.403
C: Feed	2	0.01268	5.59%	0.012831	0.006416	2.28	0.218
A * B	4	0.05501	24.23%	0.071956	0.017989	6.39	0.050
A * C	4	0.01080	4.76%	0.019389	0.004847	1.72	0.306
A * B * C	8	0.07164	31.56%	0.071640	0.008955	3.18	0.139
Error	4	0.01126	4.96%	0.011256	0.002814		
Total	26	0.22702	100.00%				
95% Confidence Interval, R-Sq = 95.04%							

3.4. Chip Segmentation Ratio

The chips produced during the experimental trials were also observed for capturing the segmentation of chips, as shown in Figure 10. The main individual contributor to the segmentation ratio was found to be the MQL flow rate, as shown in the Figure 9, the mean effect plots for the segmentation ratio. Figure 10a–c also show a higher variation in segmentation by varying the MQL flow rate. The cutting speed and feed were ranked lower than the MQL flow rate. Table 12 showed ANOVA results for the contribution of individual parameters towards the segmentation ratio with the percentage contribution of 19.68% for the MQL flow rate, 5.06% for the cutting speed, and 2.97% for feed. The dominant role of the MQL flow rate towards segmentation can be linked with the improvement of heat transfer and better temperature control during the cutting process. Figure 10d–f show the representative condition for varying feed rates. It can be seen that the effect was smaller on the segmentation ratio.

(**a**) 40 mL/ hr, 250 m/ min, 0.3 mm/ rev

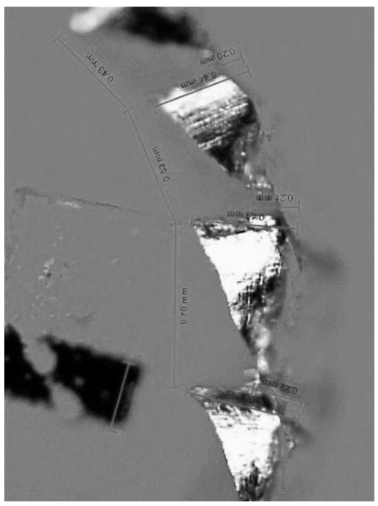

(**b**) 80 mL/ hr, 250 m/ min, 0.3 mm/ rev

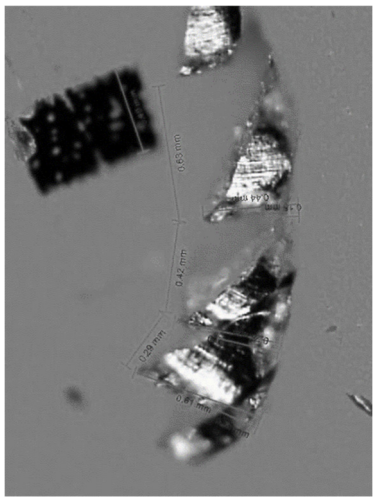

(**c**) 120 mL/ hr, 250 m/ min, 0.3 mm/ rev

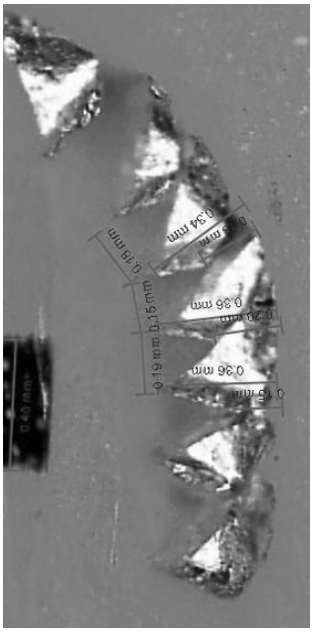

(**d**) 40 mL/ hr, 200 m/ min, 0.3 mm/ rev

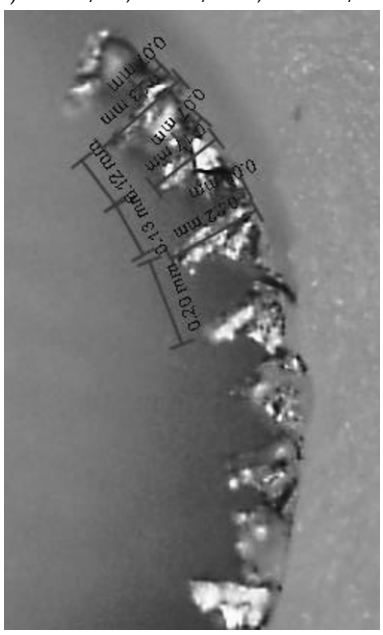

(**e**) 40 mL/ hr, 200 m/ min, 0.4 mm/ rev

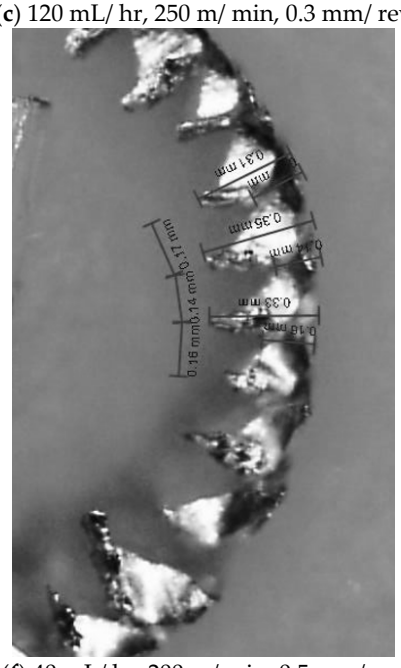

(**f**) 40 mL/ hr, 200 m/ min, 0.5 mm/ rev

Figure 10. Optical micrographs of the chips showing the influence of the MQL flow rate (**a**–**c**) and feed rate (**d**–**f**).

Table 12. Analysis of variance for the transformed response.

Source	DF	Seq SS	Contribution	Adj SS	Adj MS	F-Value	*p*-Value
A: MQL	2	0.023596	19.68%	0.015465	0.007732	4.37	0.098
B: Cutting Speed	2	0.006070	5.06%	0.009190	0.004595	2.60	0.189
C: Feed	2	0.003557	2.97%	0.001430	0.000715	0.40	0.692
A * C	4	0.022416	18.69%	0.007807	0.001952	1.10	0.463
B * C	4	0.032207	26.86%	0.022962	0.005740	3.25	0.140
A * B * C	8	0.024991	20.84%	0.024991	0.003124	1.77	0.305
Error	4	0.007072	5.90%	0.007072	0.001768		
Total	26	0.119910	100.00%				
95% Confidence Interval, R-Sq = 94.01%							

4. Conclusions and Future Suggestions

The current study investigated chip morphology and tool wear parameters during the orthogonal high-speed turning of AZ91 magnesium alloy using a biodegradable vegetable oil-based cutting fluid delivered through an MQL technique. A full factorial experimental design was formulated using the MQL flow rate, cutting speed, and feed rate as input parameters and flank wear, land width, chip contact length, saw-tooth pitch, chip compression ratio, chip segmentation ratio, and shear angle as output parameters. A GRA was conducted to determine and investigate the optimum cutting parameters based on the regarded output parameters. Through the analysis of the results, the following conclusions were drawn:

- The optimal control parameters predicted and experimentally confirmed were an MQL flow rate of 40 mL/h, cutting speed of 300 m/min, and feed rate of 0.3 mm/rev;
- The usage of said optimal parameters results in a grey relational grade improvement of 0.2675 in comparison to the referenced first experimental run;
- Using the variance analysis conducted by the Minitab program, the MQL was regarded as one of the critical variables in the optimization process with a contribution of 20%. This signifies the important role of the cooling and lubrication effects provided by the usage of the MQL in reducing tribological friction forces and cutting temperatures;
- The third level interaction of the MQL with the cutting speed and feed, and the second level interaction of the MQL flow rate with the cutting speed were found to be significant contributing factors with a contribution of 31.56% and 24.23%, respectively;
- The main individual contributor to the segmentation ratio was found to be the MQL flow rate with a percentage contribution of 19.68%. This is linked with the improved heat transfer as the MQL flow rate increased;
- For a greater assessment of the application of vegetable oil-based cutting fluids (VCFs), it is recommended that further output responses, such as surface quality, microhardness, and microstructure, are investigated during the high-speed orthogonal cutting of magnesium alloys to allow for the proper assessment of their feasibility and applicability.

Author Contributions: Conceptualization, S.P.; Methodology, A.A. and A.N.; Validation, A.A. and A.N.; Formal analysis, A.A. and S.P.; Data curation, A.A.; Writing—original draft, A.A.; Writing—review & editing, S.P. All authors have read and agreed to the published version of the manuscript.

Funding: Rochester Institute of Technology – Dubai Campus (Internal Research Grant).

Data Availability Statement: The data presented in this study are available on request from corresponding author.

Conflicts of Interest: The authors declare no conflict of interest.

References

1. Gándara, M.J.F. Recent growing demand for magnesium in the automotive industry recent growing demand for magnesium in the automotive industry. *Mater. Technol.* **2011**, *45*, 633–637.
2. Overview Magnesium for Automotive Applications. Available online: www.tms.org/jom.html (accessed on 10 September 2022).
3. Ramalingam, V.V.; Ramasamy, P.; Das Kovukkal, M.; Myilsamy, G. Research and Development in Magnesium Alloys for Industrial and Biomedical Applications: A Review. *Met. Mater. Int.* **2020**, *26*, 409–430. [CrossRef]
4. Li, N.; Zheng, Y. Novel Magnesium Alloys Developed for Biomedical Application: A Review. *J. Mater. Sci. Technol.* **2013**, *29*, 489–502. [CrossRef]
5. Wan, Y.; Xiong, G.; Luo, H.; He, F.; Huang, Y.; Zhou, X. Preparation and characterization of a new biomedical magnesium-calcium alloy. *Mater. Des.* **2008**, *29*, 2034–2037. [CrossRef]
6. Ostrovsky, I.; Henn, Y. Present state and future of magnesium application in aerospace industry. In Proceedings of the International Conference "New Challenges in Aeronautics" ASTEC, Moscow, Russia, 19–22 August 2007; Volume 7, pp. 19–22.
7. Nadanasabapathi, S.; Viswanathan, R.; Sivashankar, N.; Chandrakumar, S.; Karthik, R. Improving corrosion resistance of magnesium alloy for aerospace applications. *Int. J. Mech. Prod.* **2019**, *9*, 769–774. Available online: http://www.tjprc.org/publishpapers/2-67-1557740616-86IJMPERDJUN201986.pdf (accessed on 10 September 2022).
8. Wang, M.; Xiao, D.; Liu, W. Effect of Si addition on microstructure and properties of magnesium alloys with high Al and Zn contents. *Vacuum* **2017**, *141*, 144–151. [CrossRef]
9. Jayasathyakawin, S.; Ravichandran, M.; Baskar, N.; Chairman, C.A.; Balasundaram, R. Mechanical properties and applications of Magnesium alloy—Review. *Mater. Today Proc.* **2020**, *27*, 909–913. [CrossRef]
10. Chen, J.; Tan, L.; Yu, X.; Etim, I.P.; Ibrahim, M.; Yang, K. Mechanical properties of magnesium alloys for medical application: A review. *J. Mech. Behav. Biomed. Mater.* **2018**, *87*, 68–79. [CrossRef] [PubMed]
11. Guo, S.; Liu, R.; Jiang, X.; Zhang, H.; Zhang, D.; Wang, J.; Pan, F. Statistical Analysis on the Mechanical Properties of Magnesium Alloys. *Materials* **2017**, *10*, 1271. [CrossRef]
12. Catherine, L.D.K.; Hamid, D.A. Mechanical Properties and Machinability of Magnesium Alloy AZ31 and AZ91—A Comparative Review. *IOP Conf. Ser. Mater. Sci. Eng.* **2021**, *1062*, 012054. [CrossRef]
13. Viswanathan, R.; Ramesh, S.; Maniraj, S.; Subburam, V. Measurement and multi-response optimization of turning parameters for magnesium alloy using hybrid combination of Taguchi-GRA-PCA technique. *Meas. J. Int. Meas. Confed.* **2020**, *159*, 107800. [CrossRef]
14. Shi, K.; Zhang, D.; Ren, J.; Yao, C.; Huang, X. Effect of cutting parameters on machinability characteristics in milling of magnesium alloy with carbide tool. *Adv. Mech. Eng.* **2016**, *8*, 1687814016628392. [CrossRef]
15. Ramesh, S.; Viswanathan, R.; Ambika, S. Measurement and optimization of surface roughness and tool wear via grey relational analysis, TOPSIS and RSA techniques. *Meas. J. Int. Meas. Confed.* **2016**, *78*, 63–72. [CrossRef]
16. Tönshoff, H.; Winkler, J. The influence of tool coatings in machining of magnesium. *Surf. Coat. Technol.* **1997**, *94-95*, 610–616. [CrossRef]
17. Wang, J.; Liu, Y.; An, J.; Wang, L. Wear mechanism map of uncoated HSS tools during drilling die-cast magnesium alloy. *Wear* **2008**, *265*, 685–691. [CrossRef]
18. Carou, D.; Rubio, E.M.; Davim, J.P. Machinability of Magnesium and Its Alloys: A Review. In *Traditional Machining Processes. Materials Forming, Machining and Tribology*; Davim, J., Ed.; Springer: Berlin/Heidelberg, Germany. [CrossRef]
19. Nasr, M.N.; Outeiro, J. Sensitivity Analysis of Cryogenic Cooling on Machining of Magnesium Alloy AZ31B-O. *Procedia CIRP* **2015**, *31*, 264–269. [CrossRef]
20. Zakaria, M.S.; Mustapha, M.; Azmi, A.I.; Ahmad, A.; Danish, M.; Rubaiee, S. Machinability investigations of AZ31 magnesium alloy via submerged convective cooling in turning process. *J. Mater. Res. Technol.* **2022**, *19*, 3685–3698. [CrossRef]
21. Fang, F.; Lee, L.; Liu, X. Mean flank temperature measurement in high speed dry cutting of magnesium alloy. *J. Mater. Process. Technol.* **2005**, *167*, 119–123. [CrossRef]
22. Viswanathan, R.; Ramesh, S.; Subburam, V. Measurement and optimization of performance characteristics in turning of Mg alloy under dry and MQL conditions. *Meas. J. Int. Meas. Confed.* **2018**, *120*, 107–113. [CrossRef]
23. Cagan, S.C.; Buldum, B.B.; Özkul, I. Farklı İşleme Koşullarında AZ91D Magnezyum Alaşımının Tornalanmasında Talaş Morfolojisi. *Süleyman Demirel Üniversitesi Fen Bilim. Enstitüsü Derg.* **2019**, *23*, 108–114. [CrossRef]
24. Sankaranarayanan, R.; Krolczyk, G.M. A comprehensive review on research developments of vegetable-oil based cutting fluids for sustainable machining challenges. *J. Manuf. Process.* **2021**, *67*, 286–313. [CrossRef]
25. Sarikaya, M.; Gupta, M.K.; Tomaz, I.; Danish, M.; Mia, M.; Rubaiee, S.; Jamil, M.; Pimenov, D.Y.; Khanna, N. Cooling techniques to improve the machinability and sustainability of light-weight alloys: A state-of-the-art review. *J. Manuf. Process.* **2021**, *62*, 179–201. [CrossRef]
26. Kazeem, R.A.; Fadare, D.A.; Ikumapayi, O.M.; Adediran, A.A.; Aliyu, S.J.; Akinlabi, S.A.; Jen, T.-C.; Akinlabi, E.T. Advances in the Application of Vegetable-Oil-Based Cutting Fluids to Sustainable Machining Operations—A Review. *Lubricants* **2022**, *10*, 69. [CrossRef]
27. Katna, R.; Suhaib, M.; Agrawal, N. Nonedible vegetable oil-based cutting fluids for machining processes—a review. *Mater. Manuf. Process.* **2020**, *35*, 1–32. [CrossRef]

28. Akyuz, B. A study on wear and machinability of AZ series (AZ01-AZ91) cast magnesium alloys. *Kov. Mater.* **2014**, *52*, 255–262. [CrossRef]
29. Kuczmaszewski, J.; Zagorski, I.; Gziut, O.; Legutko, S.; Krolczyk, G.M. Chip fragmentation in the milling of AZ91HP magnesium alloy. *Stroj. Vestn. J. Mech. Eng.* **2017**, *63*, 628–642. [CrossRef]
30. Pradeepkumar, M.; Venkatesan, R.; Kaviarasan, V. Evaluation of the surface integrity in the milling of a magnesium alloy using an artificial neural network and a genetic algorithm. *Mater. Tehnol.* **2018**, *52*, 367–373. [CrossRef]
31. Zhang, Z.; Liang, X.; Chen, Y.; Xu, B. Abrasion Resistance of Al-Ni-Mm-Fe Amorphous and Nanocrystalline Composite Coating on the Surface of AZ91 Magnesium Alloy. *Phys. Procedia* **2013**, *50*, 156–162. [CrossRef]
32. Tan, M.; Liu, Z.; Quan, G. Effects of Hot Extrusion and Heat Treatment on Mechanical Properties and Microstructures of AZ91 Magnesium Alloy. *Energy Procedia* **2012**, *16*, 457–460. [CrossRef]
33. Behera, B.C.; Chetan, S.G.; Paruchuri, V.R. Study of saw-tooth chip in machining of Inconel 718 by metallographic technique. *Mach. Sci. Technol.* **2019**, *23*, 431–454. [CrossRef]
34. Pervaiz, S.; Kannan, S.; Anwar, S.; Huo, D. Machinability analysis of dry and liquid nitrogen–based cryogenic cutting of Inconel 718: Experimental and FE analysis. *Int. J. Adv. Manuf. Technol.* **2022**, *118*, 3801–3818. [CrossRef]
35. Farid, A.A.; Sharif, S.; Idris, M.H. Chip morphology study in high speed drilling of Al–Si alloy. *Int. J. Adv. Manuf. Technol.* **2011**, *57*, 555–564. [CrossRef]
36. Zaghbani, I.; Songmene, V.; Khettabi, R. Fine and Ultrafine Particle Characterization and Modeling in High-Speed Milling of 6061-T6 Aluminum Alloy. *J. Mater. Eng. Perform.* **2009**, *18*, 38–48. [CrossRef]
37. Iqbal, S.A.; Mativenga, P.T.; Sheikh, M.A. A comparative study of the tool–chip contact length in turning of two engineering alloys for a wide range of cutting speeds. *Int. J. Adv. Manuf. Technol.* **2009**, *42*, 30–40. [CrossRef]
38. Sun, S.; Brandt, M.; Dargusch, M. Characteristics of cutting forces and chip formation in machining of titanium alloys. *Int. J. Mach. Tools Manuf.* **2009**, *49*, 561–568. [CrossRef]
39. Hua, J.; Shivpuri, R. Prediction of chip morphology and segmentation during the machining of titanium alloys. *J. Mater. Process. Technol.* **2004**, *150*, 124–133. [CrossRef]
40. Storchak, M.; Rupp, P.; Möhring, H.-C.; Stehle, T. Determination of Johnson–Cook Constitutive Parameters for Cutting Simulations. *Metals* **2019**, *9*, 473. [CrossRef]
41. Moraiti, M.; Belis, T.; Pappa, M.; Kyratsis, P.; Maravelakis, E.; Antoniadis, A. Chip formation characteristics in high speed machining utilizing high speed microvideography. *Acad. J. Manuf. Eng.* **2014**, *12*, 6.
42. Kouadri, S.; Necib, K.; Atlati, S.; Haddag, B.; Nouari, M. Quantification of the chip segmentation in metal machining: Application to machining the aeronautical aluminium alloy AA2024-T351 with cemented carbide tools WC-Co. *Int. J. Mach. Tools Manuf.* **2013**, *64*, 102–113. [CrossRef]
43. Davim, J.P. Application of Merchant theory in machining particulate metal matrix composites. *Mater. Des.* **2007**, *28*, 2684–2687. [CrossRef]
44. Kuo, Y.; Yang, T.; Huang, G.-W. The use of grey relational analysis in solving multiple attribute decision-making problems. *Comput. Ind. Eng.* **2008**, *55*, 80–93. [CrossRef]
45. Gok, A. A new approach to minimization of the surface roughness and cutting force via fuzzy TOPSIS, multi-objective grey design and RSA. *Meas. J. Int. Meas. Confed.* **2015**, *70*, 100–109. [CrossRef]
46. Jozić, S.; Bajić, D.; Celent, L. Application of compressed cold air cooling: Achieving multiple performance characteristics in end milling process. *J. Clean. Prod.* **2015**, *100*, 325–332. [CrossRef]